Production Engineering (2023) 17:773–783
https://doi.org/10.1007/s11740-023-01191-w

QUALITY

Automated geometry characterization of laser-structured battery electrodes

Lucas Hille[1] · Paul Hoffmann[1] · Johannes Kriegler[1] · Andreas Mayr[1] · Michael F. Zaeh[1]

Received: 20 January 2023 / Accepted: 28 February 2023 / Published online: 25 April 2023

Abstract
Micro structuring of battery electrodes with pulsed laser radiation substantially increases the performance of lithium-ion batteries. For process design and monitoring, determining the resulting hole diameters and depths is essential. This study presents an automated, model-based approach for the geometry characterization of laser-drilled structures in battery electrodes. An iteratively re-weighted least squares algorithm is used for fitting of a reference plane to confocal laser scanning microscopy images of laser-structured electrodes. Using a threshold-based segregation of the generated weights, the holes are segmented from the pristine electrode surfaces. The results from the automated geometry determination were found to coincide well with manual measurements. By reducing the image resolution, the runtime of the code could be decreased, which yet lowered the accuracy of the hole depth prediction. In a sensitivity analysis, the algorithm performed stably under changes in the recording conditions, such as altered image brightness, frame rate, or vertical resolution. In conclusion, the presented method reduces the effort and increases the reproducibility for analyzing large experimental data sets in laser electrode structuring. Furthermore, the approach can be successfully transferred to other applications, which is demonstrated by indentations in battery current collector foils stemming from electrode calendering.

Keywords Laser structuring · Electrode manufacturing · Battery production · Image processing · Geometry determination

1 Introduction

Lithium-ion batteries (LIBs) are the cornerstone of the mobility sector's transition from internal combustion engines toward electric mobility. Hence, large production capabilities for LIBs are currently being built up, especially in Asia, North America, and Europe [1]. Laser structuring of LIB electrodes is a novel process in battery production, enabling electrochemical performance improvements of LIBs. It was shown that microscopic holes drilled in the electrode coatings (compare Fig. 1) enhance the fast charging capability [2] and increase the lifetime of LIBs [3, 4]. The electrochemical benefits are especially pronounced when laser structuring is applied to graphite anodes [5] and to thick [6] or highly compacted electrodes [7]. Furthermore, the process step of electrolyte filling can be accelerated by laser structuring as this facilitates the wetting of the electrodes with electrolyte [8, 9].

Currently, laser structuring of battery electrodes is not applied in industrial battery production due to several challenges, such as its integration into the manufacturing process chain [10] and scaling issues [11]. Furthermore, process design is highly time-consuming because of non-linear interdependencies between the laser process parameters and the resulting hole geometries [12, 13]. Electrodes are composed of different-sized active material particles incorporated in a polymer binder matrix presenting a heterogeneous material structure. Thus, material ablation by laser radiation is a complex process generating statistically deviating drillings (compare Fig. 1). For optimized electrochemical performance, the introduced holes should exhibit low diameters and large depths resulting in high aspect ratios [14]. Their geometries are usually characterized using topographic microscopy methods for creating electrode surface images, such as confocal laser scanning microscopy (LSM) [10] or white light interferometry (WLI) [13]. Typically, the holes' diameters and depths are determined manually based on line or area profiles. The procedures are highly time-consuming

✉ Lucas Hille
lucas.hille@iwb.tum.de

1 Technical University of Munich, Germany; TUM School of Engineering and Design, Department of Mechanical Engineering, Institute for Machine Tools and Industrial Management, Munich, Germany

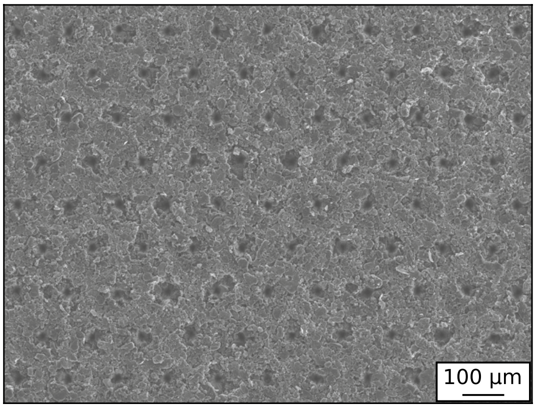

Fig. 1 Scanning electron microscopy (SEM) image of a laser-structured graphite anode

and lack reproducibility as the geometries for measurement have to be fitted manually by the operator.

Since laser structuring is not yet implemented in industrial battery production lines [10], literature addressing the automated sensor data analysis for design and monitoring of the process is scarce. Nevertheless, approaches for the image analysis of sensors capturing a substrate's topography are known from other fields of production engineering. Ye et al. developed a method for the characterization of weld beads using a laser line profile sensor with model-based classification [15]. In their approach, they considered surface curvatures of the samples by fitting a polynomial model to the topographic data and located the weld bead using a threshold-based approach depending on the noise level of the data. Using LSM, Ismail et al. measured and quantified the surface structure and periodicity of tissue paper based on the analytical detection of waviness along the sample [16]. They pointed out that in contrast to other measurement methods, LSM has the potential to be used directly in the production line due to its accuracy and simplicity. Besides the application in production engineering, the automated analysis of topography data is known from other disciplines, such as medicine [17] and geography [18].

The approaches presented above indicate the feasibility of an automated analysis of topographic image data, but are not directly transferable to laser electrode structuring due to the unique surface morphology of laser-structured battery electrodes. Therefore, an approach for the automated evaluation of laser-structured hole geometries is presented in this study. The method substantially reduces the time for process design and increases the transferability of the obtained results. Furthermore, the proposed procedure is not limited to LSM images taken for the sake of process design but can similarly be applied for in-line process monitoring based on any sensor generating topographic data, such as a laser line scanner.

2 Experimental set-up

2.1 Sample preparation

Various graphite anodes of different compositions and thicknesses stemming from the in-house battery production line at the Institute for Machine Tools and Industrial Management (*iwb*) of TU Munich [19] were used as samples in this study. 15 electrodes were used for benchmarking, runtime evaluation, and sensitivity analyses (compare Sect. 4). They were structured with a nanosecond-pulsed ytterbium fiber laser source (YLPP-1-150V-30, IPG Photonics, USA) emitting radiation at a wavelength of 1064 nm and a focal beam diameter of approx. 27 µm. For the application example (compare Sect. 5.1), 1879 graphite anodes were structured using a picosecond-pulsed laser source (Picoblade 3, Lumentum, USA) with three different discrete wavelengths (1064 nm, 532 nm, and 355 nm) and a focal beam diameter of approx. 16 µm. In both cases, a high diversity of hole diameters and depths resulted from a large variety of applied process parameters.

2.2 Laser scanning microscopy

Images of the laser-structured electrodes were recorded using a 3D laser scanning confocal microscope (VK-X 1000, Keyence, Japan). The topography of the electrode surfaces was captured with the confocal laser height measurement method using an objective with 20-fold magnification corresponding to a total magnification of 480. As a result, an image region of 704 µm × 528 µm was recorded with a resolution of 1024 px × 768 px. In the according measurement software (VK-H2X, Keyence, Japan), the illumination was set to 75% of the maximum illumination strength and a vertical scan step size of 0.75 µm was used. The "ultra high speed" measurement condition with an image acquisition frame rate of 15 Hz was applied. For a sensitivity analysis, the illumination strength, the magnification, the frame rate, and the vertical step size of the confocal measurement were altered.

2.3 Manual geometry determination

The manual geometry characterization was performed using the native analysis software of the LSM setup (MultiFileAnalyzer, Keyence, Japan). The holes' diameters and depths can be measured based on one or several line cuts through the electrode topography. These are evaluated by

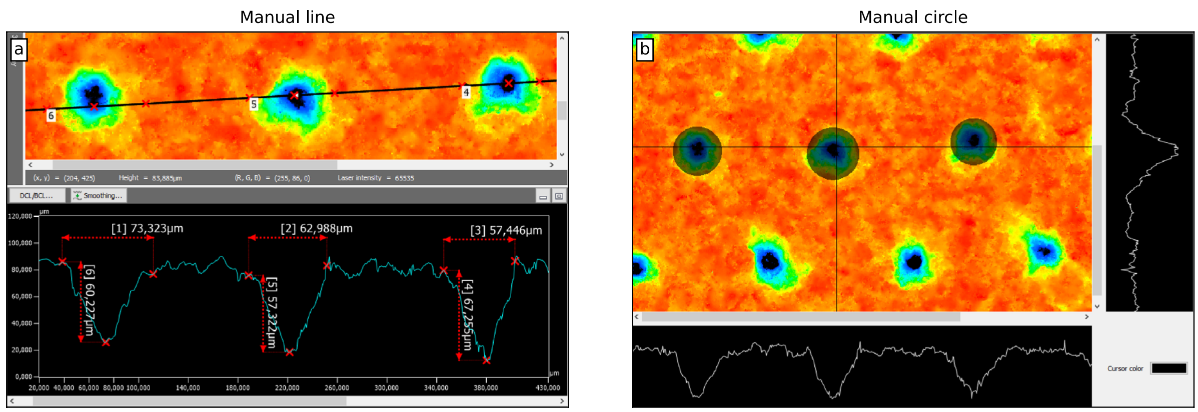

Fig. 2 Manual geometry determination using the native analysis software of the LSM setup (MultiFileAnalyzer, Keyence, Japan) based on line (**a**) and circle (**b**) profiles demonstrated at an exemplary laser scanning microscopy topography image. In the "Manual line" method (**a**), a line cut through the electrode topography is manually defined (upper part), from which the hole diameters and depths are measured (lower part). In the "Manual circle" method (**b**), circles resembling the holes are manually defined and evaluated regarding diameter and depth

manually defining the upper hole edges and extracting the deepest point to quantify the hole widths and depths, respectively (compare Fig. 2a). The approach, which will be referred to as "Manual line" in the following, faces several drawbacks as the line profiles are set and evaluated by a human user:

- The depths are measured with respect to a manually set reference plane, whose vertical position influences the values for the hole depth.
- The line profiles typically do not cross the deepest point of the holes, especially if several holes are analyzed, and thus tend to underestimate the hole depth.
- The deviation of the holes from a circular shape results in a high dependence of the measured hole diameters on the line profile positioning.
- The hole edges may be interpreted incongruently by different users as the transition from "hole" to "no hole" is typically gradual and seamless.
- Analyzing the topographies is a time-intensive task since the line profiles are set by hand and the diameters and depths are measured manually for each hole.

Alternatively, circles resembling the holes can be defined (compare Fig. 2b). While the hole diameters can be directly obtained from these circles, the hole depth is extracted as the minimum height value within the circle area with respect to a pre-defined reference plane. The method will be referred to as "Manual circle" in the following. This approach is also time-consuming and prone to errors as the concordance of the circle with the non-circular holes can vary between users due to an individual interpretation of the holes' edges. Furthermore, the problems arising from a manually defined reference plane mentioned above remain unaltered.

2.4 Implementation of the automated approach

The method for the automated geometry determination was implemented using Python 3.8 with the programming libraries NumPy and SciPy for data processing and analysis. The code was executed on a standard notebook with 16 GB of random-access memory (RAM) and a 4-core central processing unit (CPU) with 1.8 GHz (Core i7-8550U, Intel, USA).

3 Approach

3.1 Data import and pre-processing

Initially, the height images exported from the LSM analysis software in a comma-separated value (CSV) file format are imported and plotted as a pseudo-color image (compare Fig. 3a). For smoothing purposes a 3 px × 3 px median filter is applied to the image data due to its beneficial edge preservation properties at low noise levels [20].

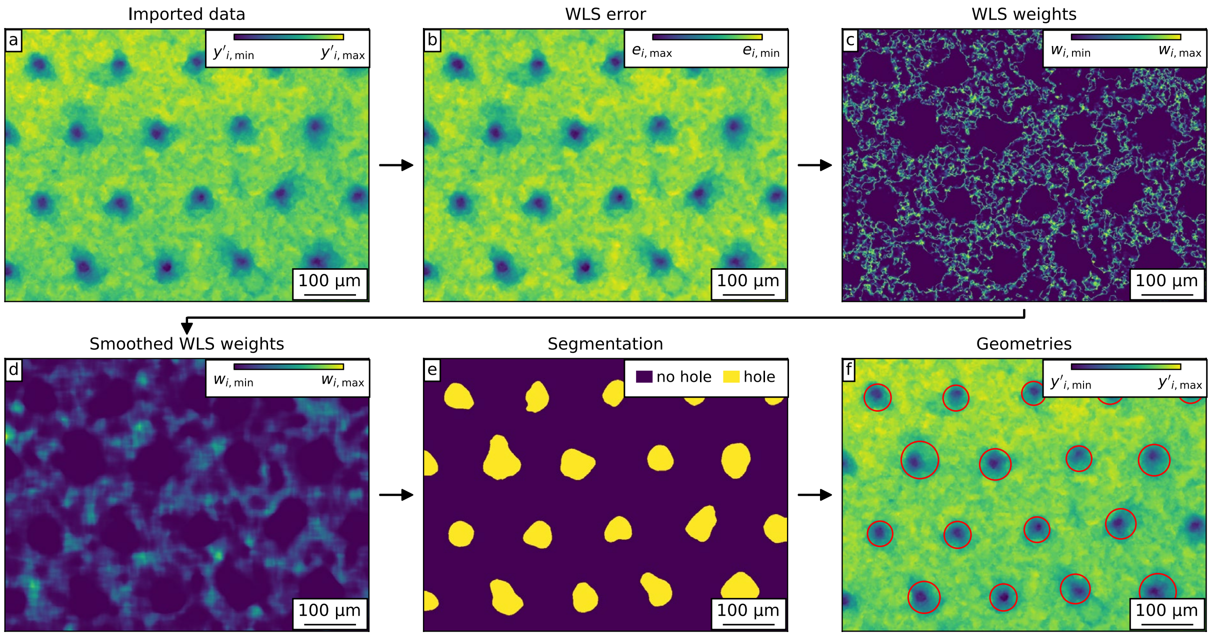

Fig. 3 The automated geometry determination procedure demonstrated at an exemplary laser scanning microscopy topography image of a laser-structured graphite anode

3.2 Reference plane modeling

Since a precise horizontal positioning of the electrode substrates cannot be guaranteed during LSM, tilted surfaces are typically observed in the recorded topography images (compare top left and bottom right of Fig. 3a). In order to avoid a misinterpretation of the geometry determination, a plane is fitted to the electrode surface, serving as a reference for the hole characterization. As bending of the substrates is typically not observed, a flat plane y can adequately resemble the electrode surfaces and no higher-order polynomials are required. For model fitting, the plane can be written in matrix notation as

$$y_i = \boldsymbol{\beta}\mathbf{X}_i \tag{1}$$

with $\boldsymbol{\beta} = (\beta_0, \beta_1, \beta_2)$ and $\mathbf{X}_i = (1, x_{1,i}, x_{2,i})^{\mathrm{T}}$ [21, Section 2.2.7]. Herein, i is the i-th pixel and thus $i \in [1, \dots, I]$ with I being the total number of measured data points. The reference plane is fitted to the measured data using an iteratively re-weighted least squares (IRLS) algorithm (compare Algorithm 1) [22]. The procedure is initialized by an ordinary least squares (OLS) approach with equal weights $w_i = 1$ for all data points. In each iteration, the weighted least squares (WLS) problem

$$\boldsymbol{\beta} = \arg\min_{\boldsymbol{\beta}} \left(\sum_{i=1}^{I} w_i (y'_i - \boldsymbol{\beta}\mathbf{X})^2 \right) \tag{2}$$

is solved by calculating [21, Section 6.8.1]

$$\boldsymbol{\beta} = \left(\mathbf{X}^{\mathrm{T}}\mathbf{W}\mathbf{X}\right)^{-1}\mathbf{X}^{\mathrm{T}}\mathbf{W}y'_i \tag{3}$$

with $\mathbf{W} = \mathrm{diag}(w_1, \dots, w_n)$. Subsequently, the error e_i between the modeled plane y_i and the measured data y'_i is calculated. The weights are updated such that a low value is assigned to pixels with a large error. This ensures that the laser-structured holes are excluded from the reference plane fitting as previously described by Ye et al. for modeling of a weld bead surface [15]. If $\sum_{i=1}^{I} w_i e_i$ falls below a pre-defined threshold value $e_{\mathrm{threshold}}$, the iteration is stopped. The matrix consisting of the final error values e_i can be interpreted as an image in which the previously tilted surface appears horizontally aligned (compare Fig. 3b).

Algorithm 1 IRLS algorithm for reference plane modeling

Set $w_i = 1$
Set $e_i = e_{\text{init}}$
Set $e_{\text{threshold}}$
while $\sum_{i=1}^{I} w_i e_i > e_{\text{threshold}}$ do
  Compute $\boldsymbol{\beta} = \left(\mathbf{X}^{\mathrm{T}}\mathbf{W}\mathbf{X}\right)^{-1}\mathbf{X}^{\mathrm{T}}\mathbf{W}_{y_i'}$
  Compute $e_i = y_i' - \beta \mathbf{X}_i$
  Compute $w_i = \exp\left(-|e_i|\right)$
End while

3.3 Data segmentation

The final weights w_i determined with the IRLS algorithm (compare Fig. 3c) are further used for segmenting the data into the two categories "hole" and "no hole". Pixels with a larger distance to the reference plane presumably corresponding to a hole are assigned a lower weight. Due to the particle-based structure of battery active materials, the electrodes exhibit a comparably high surface roughness. For this reason, a 35 px × 35 px median filter is applied to the weight matrix (compare Fig. 3d) prior to the segmentation to remove small clusters of low weights which do not represent laser-structured holes. The resulting reduction in edge sharpness was not found to negatively affect the geometry determination. The mask size of the median filter linearly scales down from 35 px × 35 px in case of a resolution reduction after import (compare Sect. 3.1). The data is finally segmented by classifying pixels with a weight below a certain threshold value as holes. This results in a binary matrix with the two categories "hole" and "no hole" (compare Fig. 3e). A threshold value of 10^{-7} was empirically determined to work well for typical hole dimensions between approx. 10 µm and 100 µm in diameter and depth, respectively. The numerical value of the threshold influences the obtained hole diameters, while the hole depths remain unaltered (compare Sect. 3.5).

3.4 Hole numbering

After the segmentation, adjacent pixels classified as holes are identified as one hole, grouped, and numbered. For this purpose, the algorithm scans the image from top to bottom and from left to right for pixels classified as holes. As soon as a hole is recognized, the adjacent area left of the pixel is checked for an already numbered hole. If a hole is detected, the pixel is assigned the hole number of the already existing pixel. Otherwise, the pixel is classified as a new hole. Holes bordering on the image edge are neglected as their diameter and depth cannot be determined correctly.

3.5 Geometry determination

For the hole diameter determination, the geometric center of each hole is determined. The hole radius equals the average distance of each edge pixel to the geometric center and is calculated using Pythagoras' theorem. For visualization of the determined diameters, a circle with the respective diameter is placed around the geometric center for each hole (compare Fig. 3f). The two pixels with the lowest height values per hole are averaged for the depth determination to eliminate the effect of outliers in the signal. The mean vertical distance of these pixels to the reference plane yields the respective hole depth.

4 Validation

4.1 Benchmark against manual geometry determination

The automated approach for geometry determination developed in this study was benchmarked against manual measurements of the hole geometries for validation purposes. For this purpose, 15 LSM images of different laser-structured battery electrodes were analyzed automatically and with the two manual methods introduced in Sect. 2.3. Care was taken to ensure a high diversity of the electrode samples regarding the diameters, depths, and pitch distances of the holes. The determined hole diameters obtained with the "Manual line" method deviated upwards and downwards, respectively, from the automated approach in all files (compare Fig. 4). In contrast to that, the "Manual circle" method did not show a clear divergence trend as it yielded higher values in eight images and lower values in seven images than the automated approach for both the diameter and the depth.

The shallower depths determined with the "Manual line" method compared to the automated and the "Manual circle" approach are ascribed to the procedure described in Sect. 2.3. As the pixels with the lowest height values seldom lie on the line cut through the topography, the deepest points of the holes are rarely covered by the "Manual line" approach. This is because the lines typically do not meet the deepest point within the holes, which are not necessarily located precisely in the hole centers. The larger diameters measured using the "Manual line" method result from the manual choice at which height the diameters are measured (compare Fig. 2a) resulting in deviations,

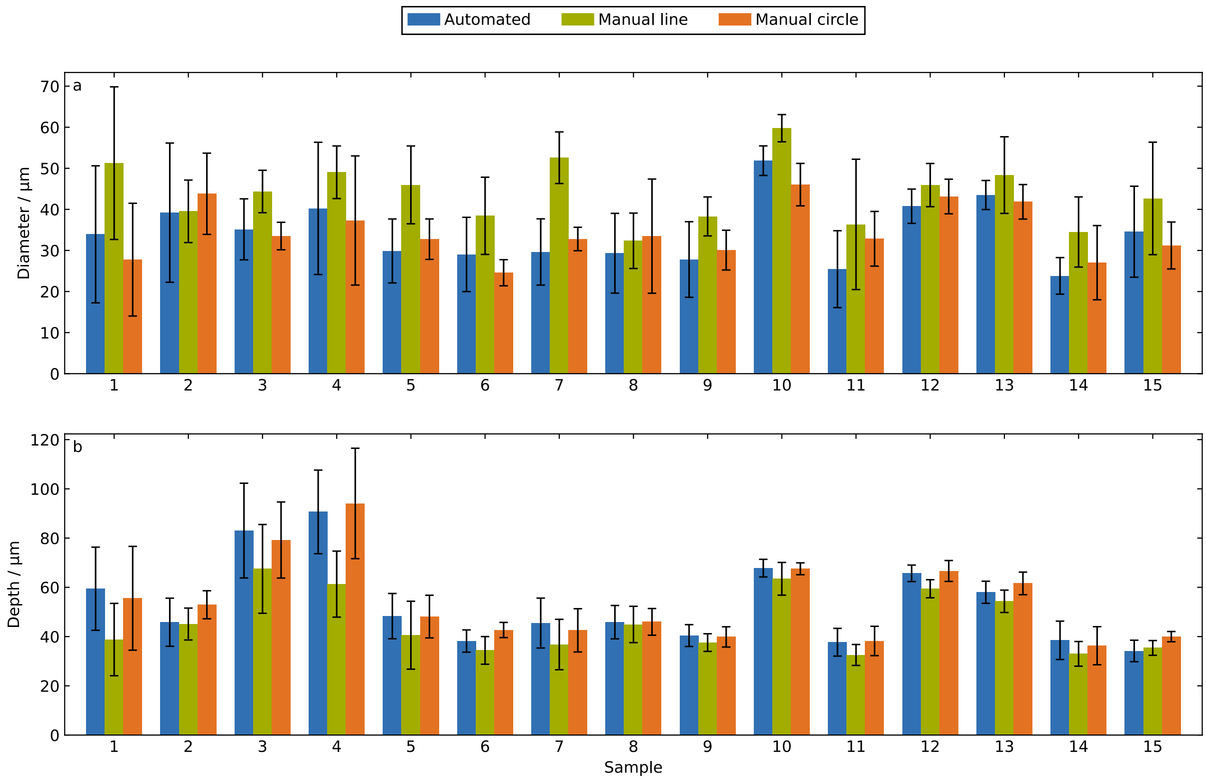

Fig. 4 Comparison of the automated geometry characterization (blue) with the manual approaches "Manual line" (orange) and "Manual circle" (green). The hole diameters (**a**) and hole depths (**b**) were determined for 15 exemplary samples with diverse hole geometries. Average and standard deviation results from all holes per sample are indicated (color figure online)

especially for conical or cascading hole geometries. The diameters determined with the "Manual circle" method are influenced by the selection of the circle size through the operator (compare Fig. 2b). The slight depth deviations between the automated approach and the "Manual circle" method presumably result from different reference planes to which the depths are referenced.

4.2 Reduction of the image resolution

For a decrease of the code runtime, the raw image resolution of 1024 px × 768 px of the 15 samples evaluated in the previous Sect. 4.1 was reduced in steps by using only every n-th row and n-th column ($n \in \mathbb{N}$) of the data matrices. From Fig. 5a, it becomes apparent that the time for the execution of the code for each sample could be significantly diminished by decreasing the image resolution. Furthermore, the algorithm determining the holes' geometric centers accounted for most of the code execution time, especially at high resolutions. This is due to the algorithm's sequential rasterizing of the whole matrix (compare Sect. 3.4), resulting in a high dependence of the computing effort on the image size. Neither the absolute values nor the spread of the obtained hole diameters was significantly influenced by a reduction of the pixel number (compare Fig. 5b). The obtained depth, in contrast, showed a clear trend toward lower values at decreased image resolutions (compare Fig. 5c). As the automated hole depth determination is based on the pixels with the lowest height value per hole (compare Sect. 3.5), a removal of image rows and columns results in a statistical erase of these pixels and thus falsifies the obtained maximum hole depths.

This suggests a trade-off between a short runtime of the code and a precise prediction of the hole depths. Since at very low image resolutions no substantial further reduction of the runtimes could be achieved (compare zoom-in inlet of Fig. 5a), but the determined hole depths kept decreasing (compare Fig. 5c), it is recommended to keep the image resolution higher than approx. 10^5 px.

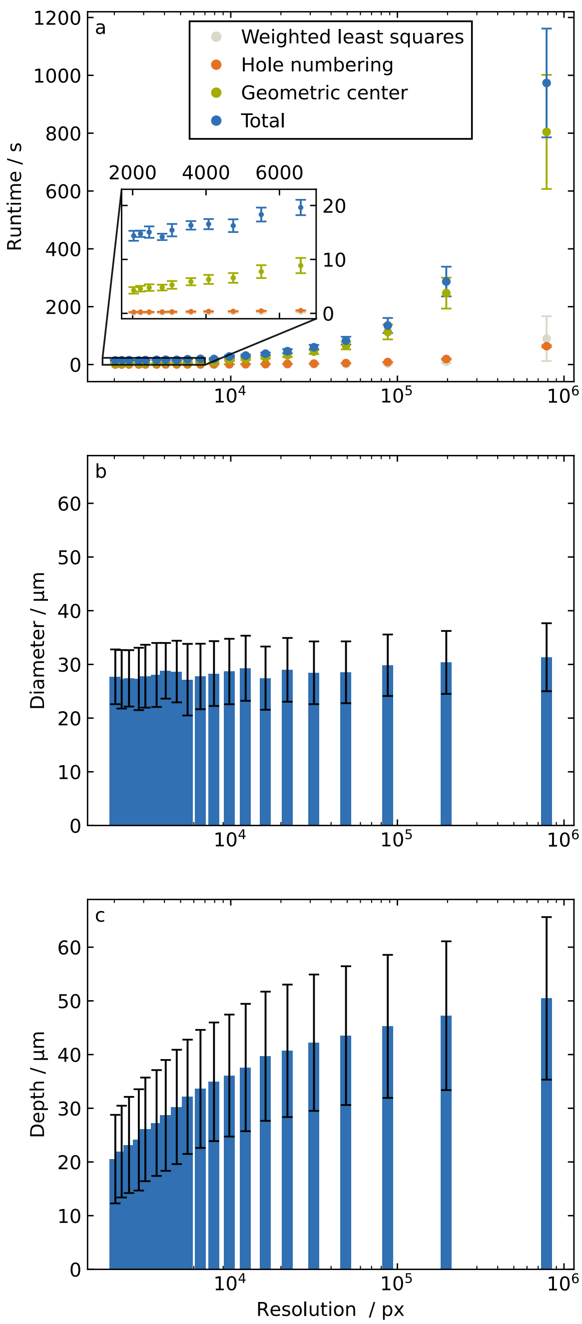

Fig. 5 Effect of an image resolution reduction on the runtime (**a**), the obtained diameters (**b**), and depths (**c**) of the automated geometry determination. Average and standard deviation results from 15 exemplary samples with diverse hole geometries are indicated

4.3 Sensitivity analysis

In order to evaluate the sensitivity of the automated geometry determination, individual recording conditions at the LSM setup were varied while the other settings were left as specified in Sect. 2.2. The obtained images of an exemplary sample were subsequently analyzed regarding the hole diameters and depths.

The confocal illumination of the probes during image capture was varied from low to high values corresponding to a lower and higher sample brightness, respectively. Whereas the illumination strength did not influence the hole diameters (compare Fig. 6a), the measured hole depths showed illumination-dependent values (compare Fig. 6e). As the dependency was observed in the automated and manual geometry determinations alike, the LSM measurement seems to yield lower depth values at a lower illumination. It is assumed that a high brightness in the holes is needed to capture the hole bottoms. The magnification of the image data was changed by using different objectives (compare Fig. 6b and f). A clear drop in the obtained hole depths was observed at high magnifications (compare Fig. 6f). Again, the dependency was present in all analyzing methods and is thus attributed to a change in the original topography data. The vertical depth of focus is presumably reduced at high magnifications, resulting in a lowered capability to capture the actual hole depths. Furthermore, the depth resolution could be diminished by a lowered illumination of the holes as the image brightness scales inversely with the lateral magnification of an objective [23, Section 2.4]. A change in the frame rate did not significantly influence the measured hole diameters and depths in any method (compare Fig. 6c and g). Also, the step size during the LSM measurement, which defines the topography data's vertical resolution, did not significantly affect the geometry values determined in automated mode or manually (compare Fig. 6d and h).

It is concluded that the automated geometry determination is robust against alterations in the recording conditions during LSM. The differences in the measured geometries by changes of the illumination or the magnification were also obtained in manual analysis. Hence, the deviations are ascribed to a variation of the original topography data and are not due to a limitation of the automated geometry determination.

5 Application

5.1 Application to a laser structuring process study

The automated geometry determination was applied to a data set consisting of 1879 topographic images obtained in the course of a comprehensive process study. In the experiments, different laser processing parameters, such as the fluence, the pulse repetition rate, or the wavelength, were varied to assess their influence on the

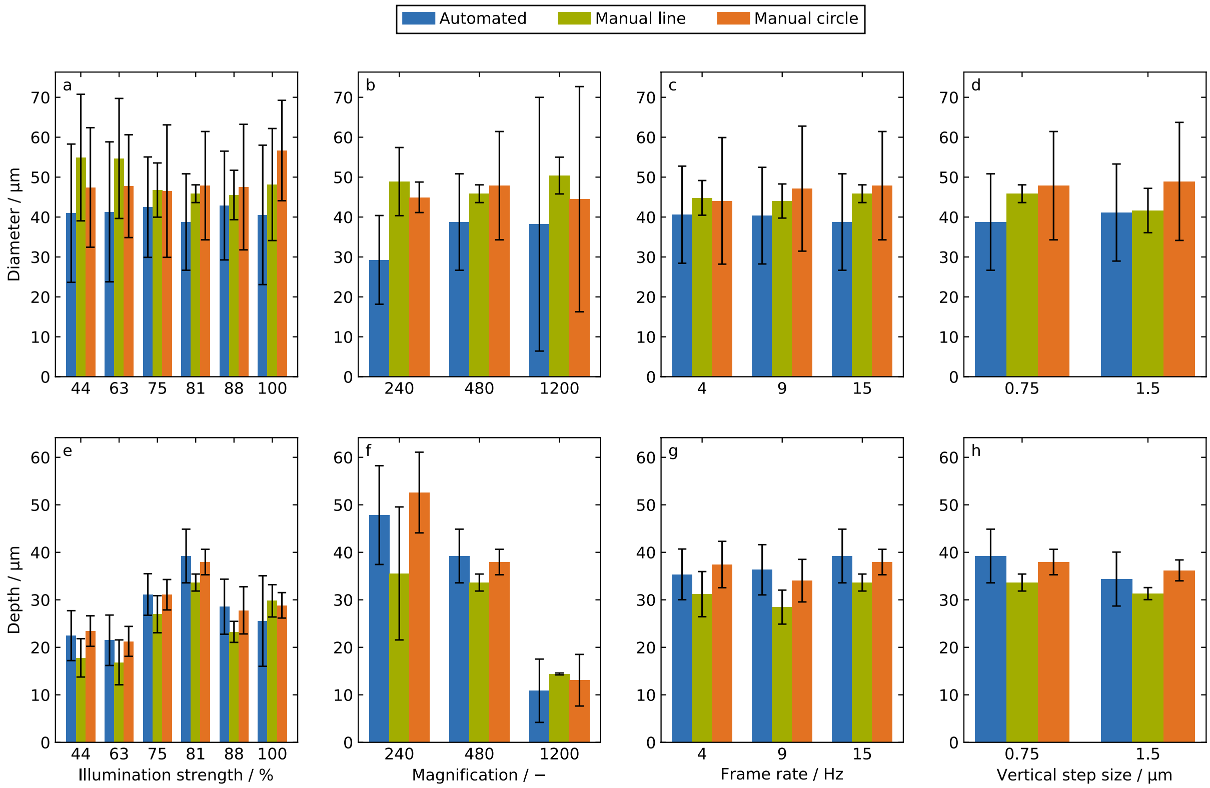

Fig. 6 Sensitivity analysis of the automated geometry determination (blue) compared to the manual approaches “Manual line” (orange) and “Manual circle” (green). The hole diameters (**a**–**d**) and hole depths (**e**–**h**) were determined under varying recording conditions. Average and standard deviation results from all holes per sample are indicated (color figure online)

obtained hole geometries. The results are used here for validating the automated geometry determination. The holes were created in a quadratic arrangement with a pitch distance of 200 µm deviating from the commonly used hexagonal pattern (compare Fig. 3) [4, 5]. Furthermore, a large spread in the hole geometries is present in the data due to the diverse process parameters. The marker color in Fig. 7 depicts the aspect ratio, i.e., the hole depth divided by the hole diameter, and thus makes it possible to quickly assess the bore hole quality. In Fig. 7, markers of larger area represent a higher standard deviation of the obtained results indicating an unstable process or a misclassification of the respective sample. Hence, nearly all of the 1879 samples seem to have been classified correctly by the automated geometry determination method. High standard deviations were observed for outliers at very low depth values, where holes are hard to distinguish from the rough electrode surface. Hence, despite the large variety in detected hole geometries and the change in pitch distance, the algorithm was able to reliably characterize the majority of holes obtained in the laser process study.

5.2 Transfer to battery electrode calendering

In order to demonstrate the versatility of the method presented in this study, the algorithm was applied to another use case from battery production. During calendering, i.e., the rolling process for compaction of the electrode coatings, particles can be pressed into the metallic current collector foils. The phenomenon is especially observed with cathode materials, e.g., lithium nickel manganese cobalt oxides (NMC), due to the firmness of the active material particles and the accompanying higher compression forces [24]. The resulting indentations need to be characterized to comprehend process product correlations. For this purpose, the electrode coatings are removed with solvents and the cavities can be measured using LSM. Since the structures are mainly created by single particles, typical hole dimensions lie in the regime of a few µm. Consequently, topography images are

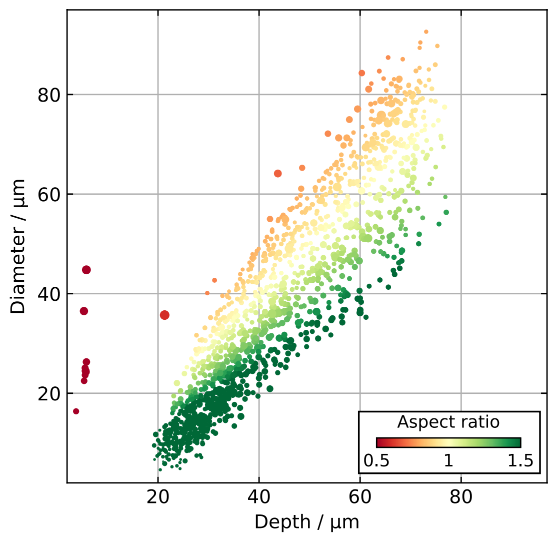

Fig. 7 Hole diameters and depths from a laser process study containing 1879 data points which were determined with the automated geometry characterization method. The marker area scales with the standard deviation, which was calculated as the mean of the diameter and depth standard deviations in the respective sample

recorded with a higher magnification than laser-structured electrodes. Thus, the 35 px × 35 px median filter applied for smoothing of the weights w_i (compare Sect. 3.3) was reduced to 5 px × 5 px to ensure that all holes are detected. Furthermore, the threshold value for segmentation (compare Sect. 3.3) was increased to 0.45 to account for the combination of small depths of the created holes and the uniformly smooth metal surface between the holes. With these slight adjustments, the indentations in the current collector foils were successfully recognized (compare Fig. 8). An average hole diameter of 2.7 µm ± 1.8 µm and an average depth of 1.2 µm ± 0.3 µm were determined. The non-regular arrangement of the holes did not pose a problem for the hole identification and geometry determination. For a widespread application of the automated geometry characterization to other use cases, it might be necessary to alter the fitted flat plane to a polynomial of higher order to account for bending of the sample surfaces. In conclusion, the developed method can be successfully transferred to other applications dealing with hole-like structures in topography data without major modifications.

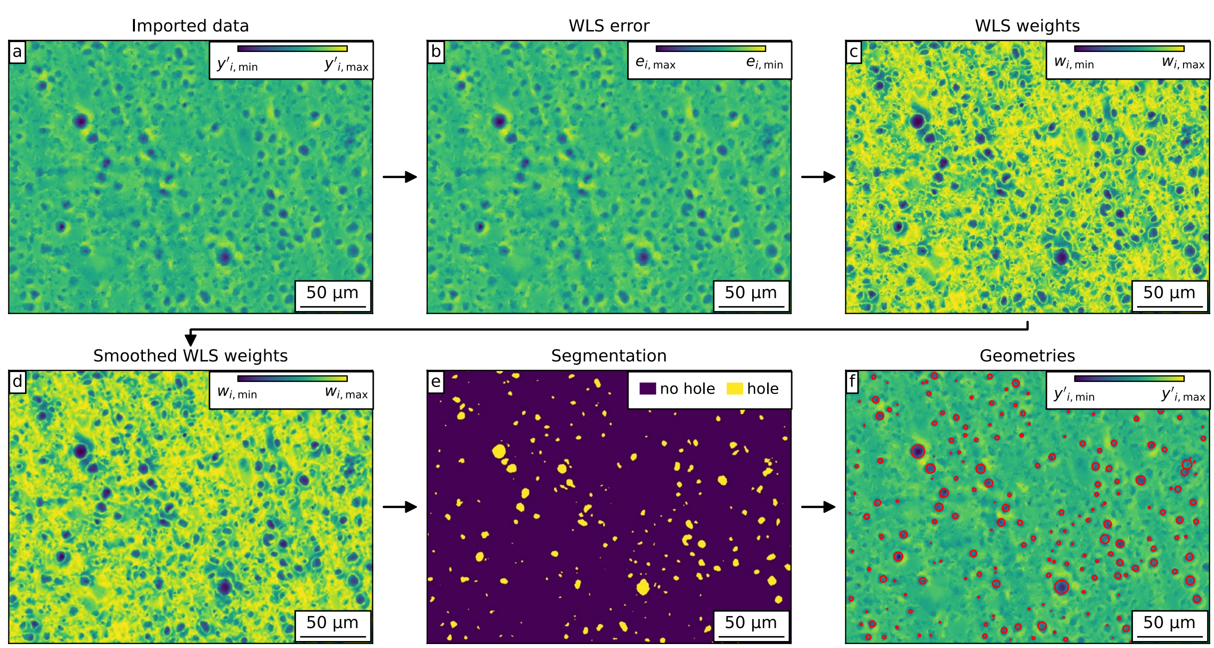

Fig. 8 Identification of indentations in an aluminum battery current collector foil using the automated approach for geometry determination. The cavities resulted from calendering of a lithium nickel manganese cobalt oxide cathode and were measured using laser scanning microscopy after removing the electrode coating

6 Conclusion

In this study, an automated approach for the geometry determination of laser-structured holes in battery electrodes was developed. In the method, topographic data of electrode surfaces stemming from 3D confocal laser scanning microscopy is initially pre-processed for noise reduction and optionally reduced in resolution to reduce the computation time. Subsequently, a reference plane is fitted to the images using an iteratively re-weighted least squares algorithm. The obtained weights are further used to segment the surfaces into the two classes “hole” and “no hole”. Finally, the holes are numbered in a rasterizing approach and the diameter and depth of each hole is determined. The presented method does not require user supervision or large training data sets. Furthermore, it can compensate for mispositioning of the workpiece during image capture resulting in inclined surfaces. The algorithm performs robustly under changing recording conditions, such as the illumination, the recording speed, or the vertical step size. An influence of the magnification and the illumination on the obtained hole geometries was observed in the automated and the manual geometry determination alike and was thus identified as an inherent limitation of laser scanning microscopy. The automated approach has proven its capability to support the process design for laser structuring of battery electrodes by reliably characterizing large and diverse data sets. A potential use of the method in process monitoring seems feasible as neither user supervision nor calibration is required. Yet, for an inline integration in industrial battery production, the runtime of the code needs to be reduced. Auspicious approaches feature a size reduction of the captured images, an efficiency increase of the code, or the use of higher computing power. Finally, the presented method is not limited to laser structuring of battery electrodes, but can be used for the characterization of hole-like structures in topographic data from other use cases, such as the detection of defects from battery electrode calendering.

Acknowledgements The financial support by the German Federal Ministry of Education and Research (BMBF) under the Grant number 03XP03316B (LaserScale) is gratefully acknowledged.

Funding Open Access funding enabled and organized by Projekt DEAL.

Data availability The datasets generated analysed during the current study are available from the corresponding author on reasonable request.

Declarations

Conflict of interest The authors declare that they have no conflict of interest.

References

1. Mauler L, Duffner F, Leker J (2021) Economies of scale in battery cell manufacturing: the impact of material and process innovations. Appl Energy 286:116499. https://doi.org/10.1016/j.apenergy.2021.116499
2. Habedank JB, Kriegler J, Zaeh MF (2019) Enhanced fast charging and reduced lithium-plating by laser-structured anodes for lithium-ion batteries. J Electrochem Soc 166(16):A3940–A3949. https://doi.org/10.1149/2.1241915jes
3. Chen K-H, Namkoong MJ, Goel V, Yang C, Kazemiabnavi S, Mortuza SM, Kazyak E, Mazumder J, Thornton K, Sakamoto J, Dasgupta N (2020) Efficient fast-charging of lithium-ion batteries enabled by laser-patterned three-dimensional graphite anode architectures. J Power Sources 471:228475. https://doi.org/10.1016/j.jpowsour.2020.228475
4. Kriegler J, Hille L, Stock S, Kraft L, Hagemeister J, Habedank JB, Jossen A, Zaeh MF (2021) Enhanced performance and lifetime of lithium-ion batteries by laser structuring of graphite anodes. Appl Energy 303:117693. https://doi.org/10.1016/j.apenergy.2021.117693
5. Hille L, Xu L, Keilhofer J, Stock S, Kriegler J, Zaeh MF (2021) Laser structuring of graphite anodes and NMC cathodes—proportionate influence on electrode characteristics and cell performance. Electrochim Acta 392:139002. https://doi.org/10.1016/j.electacta.2021.139002
6. Park J, Jeon C, Kim W, Bong S-J, Jeong S, Kim H-J (2021) Challenges, laser processing and electrochemical characteristics on application of ultra-thick electrode for high-energy lithium-ion battery. J Power Sources 482:228948. https://doi.org/10.1016/j.jpowsour.2020.228948
7. Hille L, Toepper H-C, Schriever C, Kriegler J, Keilhofer J, Noecker MP, Zaeh MF (2022) Influence of laser structuring and calendering of graphite anodes on electrode properties and cell performance. J Electrochem Soc 169(6):060518. https://doi.org/10.1149/1945-7111/ac725c
8. Habedank JB, Guenter FJ, Billot N, Gilles R, Neuwirth T, Reinhart G, Zaeh MF (2019) Rapid electrolyte wetting of lithium-ion batteries containing laser structured electrodes: in situ visualization by neutron radiography. Int J Adv Manuf Technol 102(9–12):2769–2778. https://doi.org/10.1007/s00170-019-03347-4
9. Dunlap N, Sulas-Kern DB, Weddle PJ, Usseglio-Viretta F, Walker P, Todd P, Boone D, Colclasure AM, Smith K, Tremolet de Villers BJ, Finegan DP (2022) Laser ablation for structuring Li-ion electrodes for fast charging and its impact on material properties, rate capability, Li plating, and wetting. J Power Sources 537:231464. https://doi.org/10.1016/j.jpowsour.2022.231464
10. Hille L, Noecker MP, Ko B, Kriegler J, Keilhofer J, Stock S, Zaeh MF (2023) Integration of laser structuring into the electrode manufacturing process chain for lithium-ion batteries. J Power Sources 556:232478. https://doi.org/10.1016/j.jpowsour.2022.232478

11. Habedank JB, Schwab D, Kiesbauer B, Zaeh MF (2020) Paving the way for industrial ultrafast laser structuring of lithium-ion battery electrodes by increasing the scanning accuracy. J Laser Appl 32(2):022053. https://doi.org/10.2351/7.0000078
12. Habedank JB, Endres J, Schmitz P, Zaeh MF, Huber HP (2018) Femtosecond laser structuring of graphite anodes for improved lithium-ion batteries: ablation characteristics and process design. J Laser Appl 30(3):032205. https://doi.org/10.2351/1.5040611
13. Kleefoot M-J, Sandherr J, Sailer M, Nester S, Martan J, Knoblauch V, Kumkar M, Riegel H (2022) Investigation on the parameter dependency of the perforation process of graphite based lithium-ion battery electrodes using ultrashort laser pulses. J Laser Appl 34(4):042003. https://doi.org/10.2351/7.0000757
14. Goel V, Chen K-H, Dasgupta NP, Thornton K (2023) Optimization of laser-patterned electrode architectures for fast charging of Li-ion batteries using simulations parameterized by machine learning. Energy Storage Mater 57:44–58. https://doi.org/10.1016/j.ensm.2023.01.050
15. Ye G, Guo J, Sun Z, Li C, Zhong S (2018) Weld bead recognition using laser vision with model-based classification. Robot Comput Integr Manuf 52:9–16. https://doi.org/10.1016/j.rcim.2018.01.006
16. Ismail MY, Patanen M, Kauppinen S, Kosonen H, Ristolainen M, Hall SA, Liimatainen H (2020) Surface analysis of tissue paper using laser scanning confocal microscopy and micro-computed topography. Cellulose 27(15):8989–9003. https://doi.org/10.1007/s10570-020-03399-w
17. Swindale NV, Stjepanovic G, Chin A, Mikelberg FS (2000) Automated analysis of normal and glaucomatous optic nerve head topography images. Investig Ophthalmol Vis Sci 41(7):1730–1742
18. MacMillan RA, Martin TC, Earle TJ, McNabb DH (2003) Automated analysis and classification of landforms using high-resolution digital elevation data: applications and issues. Can J Remote Sens 29(5):592–606. https://doi.org/10.5589/m03-031
19. Reinhart G, Zeilinger T, Kurfer J, Westermeier M, Thiemann C, Glonegger M (2013) Research and demonstration center for the production of large-area lithium-ion cells. In: Schuh G, Neugebauer R, Uhlmann E (eds) Future trends in production engineering. Springer, Berlin
20. Arias-Castro E, Donoho DL (2009) Does median filtering truly preserve edges better than linear filtering? Ann Stat. https://doi.org/10.1214/08-AOS604
21. Gentle JE (2007) Matrix algebra: theory, computations, and applications in statistics. SpringerLink Bücher, Springer, New York. https://doi.org/10.1007/978-0-387-70873-7
22. Wolke R, Schwetlick H (1988) Iteratively reweighted least squares: algorithms, convergence analysis, and numerical comparisons. SIAM J Sci Stat Comput 9(5):907–921. https://doi.org/10.1137/0909062
23. Nechyporuk-Zloy V (2022) Principles of light microscopy: from basic to advanced. Springer International Publishing, Cham. https://doi.org/10.1007/978-3-031-04477-9
24. Meyer C, Bockholt H, Haselrieder W, Kwade A (2017) Characterization of the calendering process for compaction of electrodes for lithium-ion batteries. J Mater Process Technol 249:172–178. https://doi.org/10.1016/j.jmatprotec.2017.05.031